



Supplement of

Detection and reconstruction of rock glacier kinematics over 24 years (2000–2024) from Landsat imagery

Diego Cusicanqui et al.

Correspondence to: Diego Cusicanqui (diego.cusicanqui@univ-grenoble-alpes.fr)

The copyright of individual parts of the supplement might differ from the article licence.

Table S1. List of medium and high resolution remote sensing data. Light grey cells correspond to the *VHR dataset*. ^(a) Corresponds to those images who have been resampled at a different resolution. ^(b) Vivero et al., 2021, McDonnel et al., 2009; ^(c) Image source from Robson et al., (2021); ^(d) Bodin X. (*unpublished*).

#	Acquisition date	Sensor-type	Raw resolution (m)	Source
1	Mars 31, 2000	Landsat 7	15	USGS (free)
2	May 31, 2000	Aerial	1	Private ^(b)
3	Mars 2, 2001	Landsat 7	15	USGS (free)
4	April 6, 2002	Landsat 7	15	USGS (free)
5	Mars 24, 2003	Landsat 7	15	USGS (free)
6	November 30, 2010	Geoeye	0.5 / 1.0*	AIRBUS/CNES ^(c)
7	Mars 23, 2012	Geoeye	0.7	AIRBUS/CNES ^(c)
8	April 12, 2013	Landsat-8	15	USGS (free)
9	April 15, 2014	Landsat-8	15	USGS (free)
10	November 18, 2014	Pleiades	0.5 / 1.0*	AIRBUS/CNES ^(d)
11	Mars 17, 2015	Landsat-8	15	USGS (free)
12	February 16, 2016	Landsat-8	15	USGS (free)
13	April 23, 2017	Landsat-8	15	USGS (free)
14	Mars 25, 2018	Landsat-8	15	USGS (free)
15	Mars 12, 2019	Landsat-8	15	USGS (free)
16	January 31, 2019	Pleiades	0.5 / 1.0*	AIRBUS/CNES ^(c)
17	Mars 31, 2020	Landsat-8	15	USGS (free)
18	Mars 1, 2020	Pleiades	0.5 / 1.0*	AIRBUS/CNES ^(c)
19	April 24, 2021	Landsat-8	15	USGS (free)
20	April 29, 2022	Landsat-8	15	USGS (free)
21	Mars15, 2023	Landsat-8	15	USGS (free)
22	January 13, 2024	Landsat-8	15	USGS (free)

Table S2. List of wrapped interferogram pairs used in this study.

Orbit	Nro	Interferogram pairs (YYYY-mm-dd)		Time span (days)	Baseline (m)
Ascending	1	2023-03-12	2023-03-24	12	-79.2558
	2	2023-03-24	2023-04-05	12	31.4153
	3	2023-04-05	2023-04-17	12	-18.7077
	4	2023-12-01	2023-12-13	12	-107.5433
	5	2023-12-13	2023-12-25	12	141.2213
	6	2023-12-25	2024-01-06	12	10.684
	7	2024-01-06	2024-01-18	12	75.0003
	8	2024-01-18	2024-01-30	12	-114.3447
	9	2024-01-30	2024-02-11	12	-20.0275
	10	2024-02-11	2024-02-23	12	-3.2986

	11	2024-02-23	2024-03-06	12	104.3847
	12	2023-04-05	2023-06-04	60	-57.0569
	13	2023-05-23	2023-07-22	60	-86.8303
	14	2023-06-16	2023-08-15	60	133.9585
	15	2023-12-01	2024-01-30	60	5.0217
	16	2023-12-13	2024-02-11	60	92.5418
	17	2023-12-25	2024-02-23	60	-51.9844
	18	2024-01-06	2024-03-06	60	41.712
	19	2023-03-12	2024-03-06	360	-36.785
	20	2023-03-24	2024-02-23	336	-61.8491
Descending	1	2022-11-27	2022-12-09	12	-100.6035
	2	2022-12-09	2022-12-21	12	-172.893
	3	2022-12-21	2023-01-02	12	136.5455
	4	2023-01-02	2023-01-14	12	-47.4244
	5	2023-01-14	2023-01-26	12	98.2317
	6	2023-01-26	2023-02-07	12	-125.1073
	7	2023-02-07	2023-02-19	12	9.516
	8	2023-02-19	2023-03-03	12	153.5736
	9	2023-03-03	2023-03-15	12	-235.122
	10	2023-03-15	2023-03-27	12	198.3794
	11	2023-03-27	2023-04-08	12	-9.3463
	12	2022-12-09	2023-02-07	60	-110.6412
	13	2022-12-21	2023-02-19	60	71.7663
	14	2023-01-02	2023-03-03	60	88.7876
	15	2023-01-14	2023-03-15	60	-98.906
	16	2023-01-26	2023-03-27	60	1.2443
	17	2023-02-07	2023-04-08	60	117.0035
	18	2023-02-19	2023-04-20	60	-107.9766
	19	2022-11-03	2023-11-22	384	60.4426
	20	2022-11-15	2023-10-17	336	4.9509

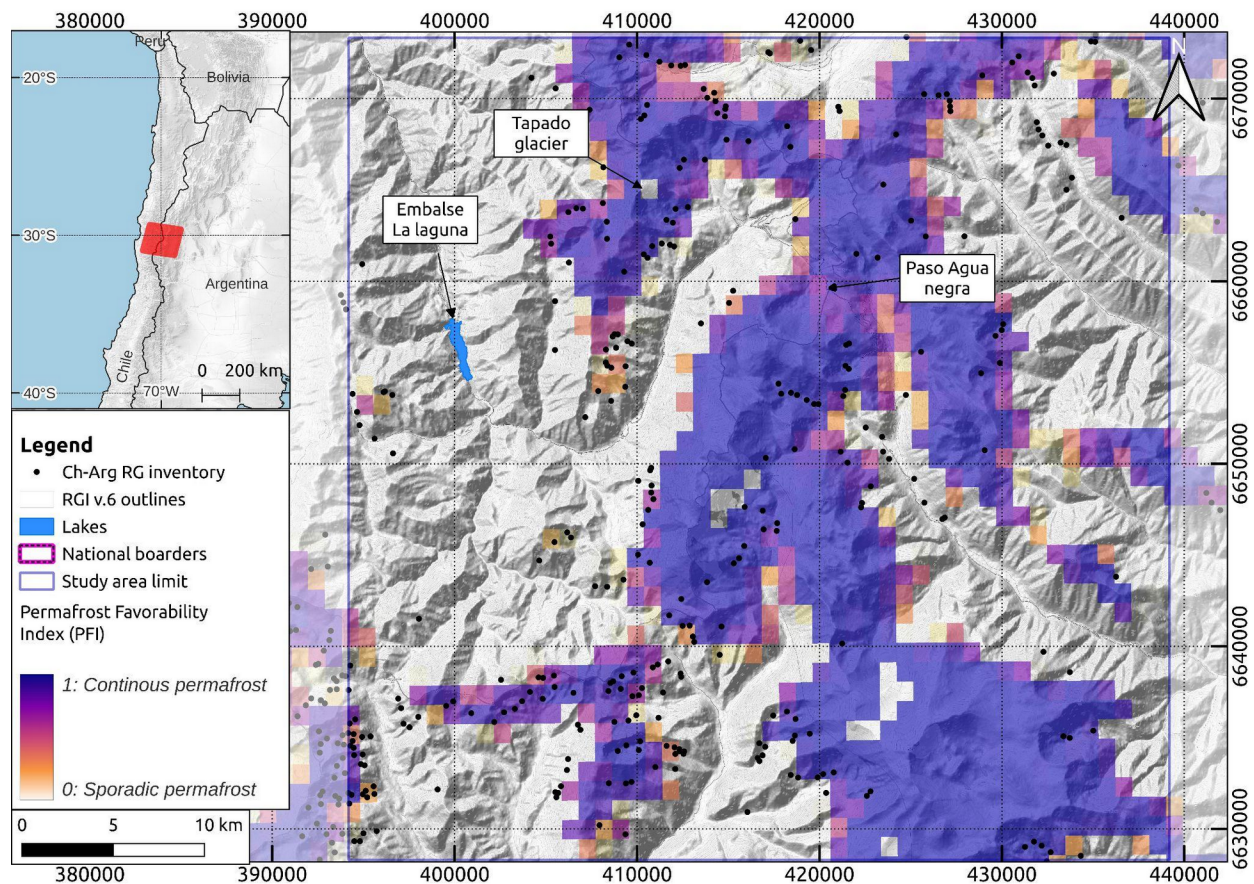


Figure S1. Location of the study area in central dry andes (between 29°20'S and 31°15'S latitude). Red square in the inner map shows the footprint of the Landsat scenes used in this study. Within the main map, black dots correspond to rock glacier inventory for Chile (DGA, 2022) and Argentina (IANIGLA, 2018). The orange-purple colorbar represents the Permafrost Favorability Index (PFI) from (Obu, 2021). Background map corresponds to © OpenTopoMap.

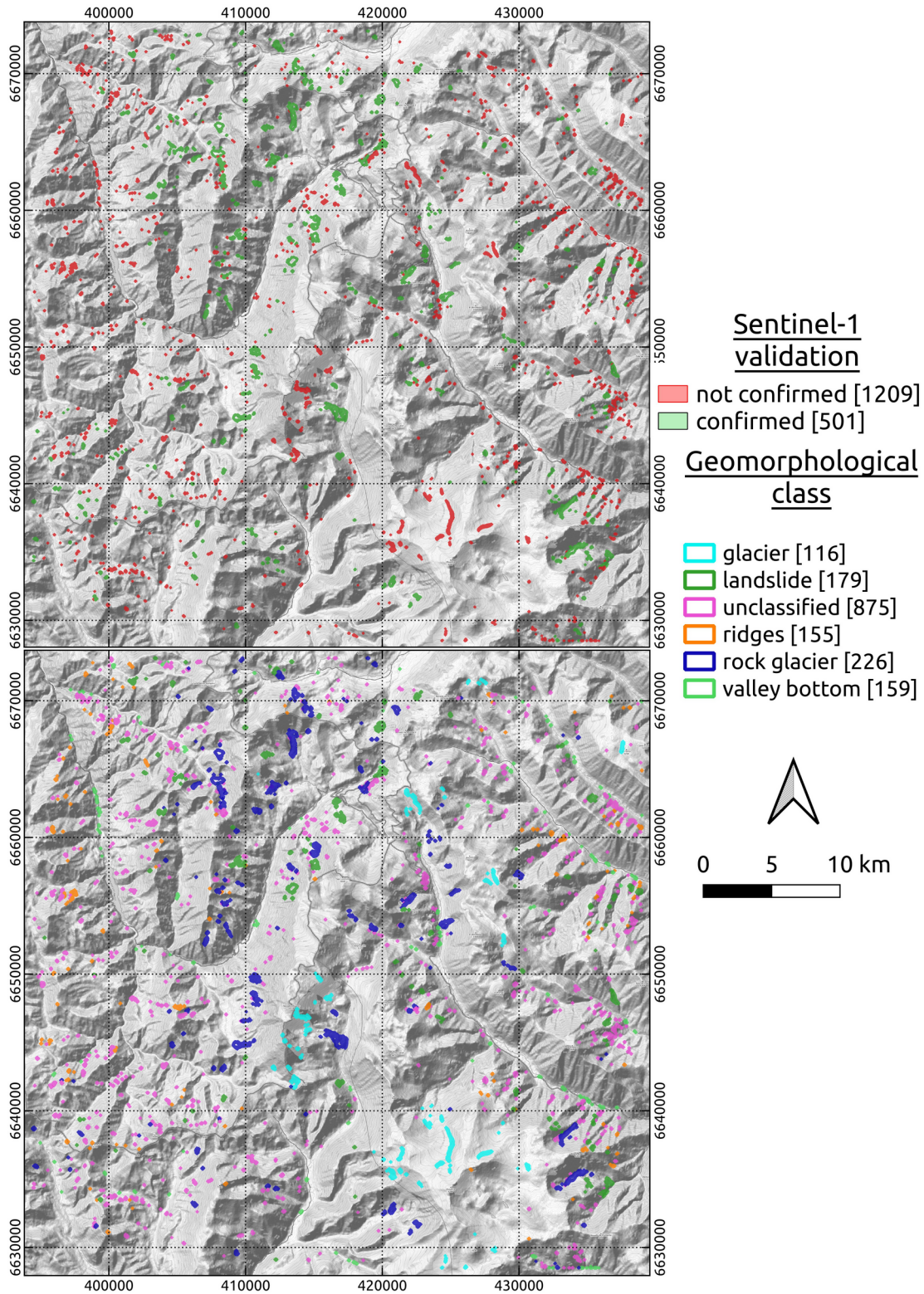


Figure S2. Spatial distribution of raw Persistent Moving Areas (PMA). Upper map shows the comparison of PMA's with InSAR wrapped interferograms. Lower map shows a geomorphological interpretation based on © GoogleEarth & © Bing high resolution WMS maps.

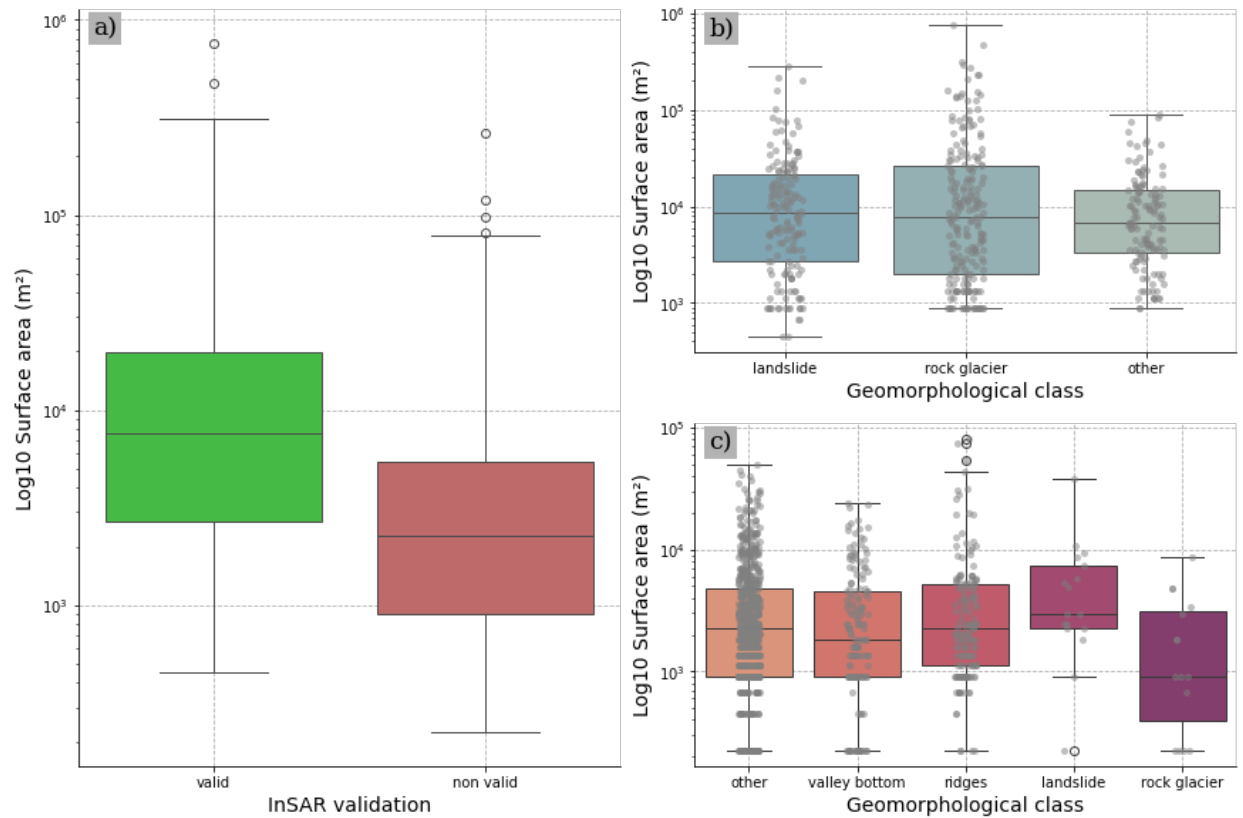


Figure S3. Boxplot representing the distribution of Persistent Moving Areas (PMA) over the study area. a) shows the distribution of valid and non-valid polygons obtained through the S1- and geomorphological validation; b) and c) shows the distribution of valid and non-valid polygons and their respective geomorphological class.

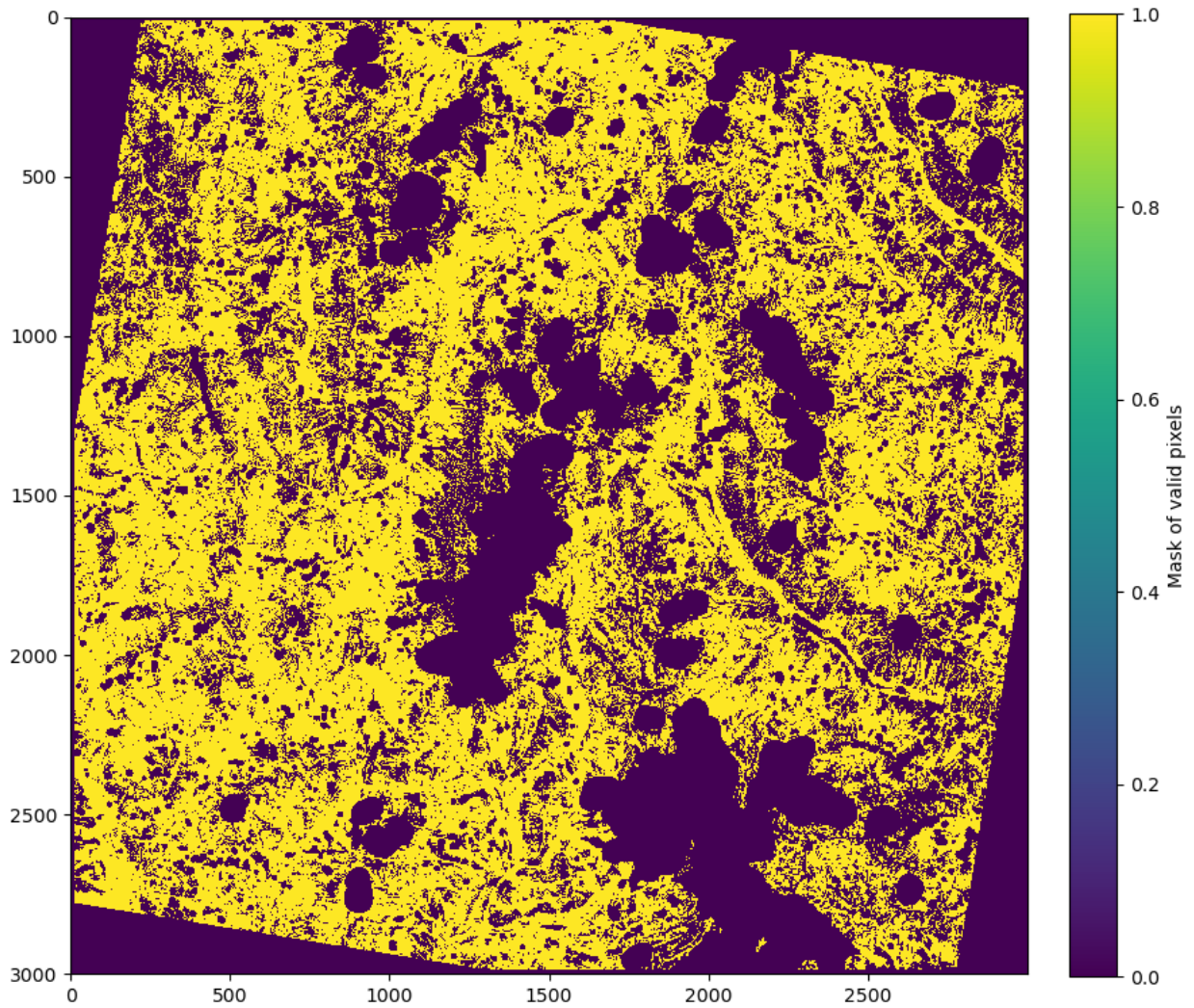


Figure S4. Mask of valid pixels used as stable areas for surface velocity uncertainty computation. For this mask, we removed slopes $> 35^\circ$, glaciers and PMA outlines. The total amount of valid pixels is 4810045, corresponding to 53% of the entire image footprint (45x45 km²).

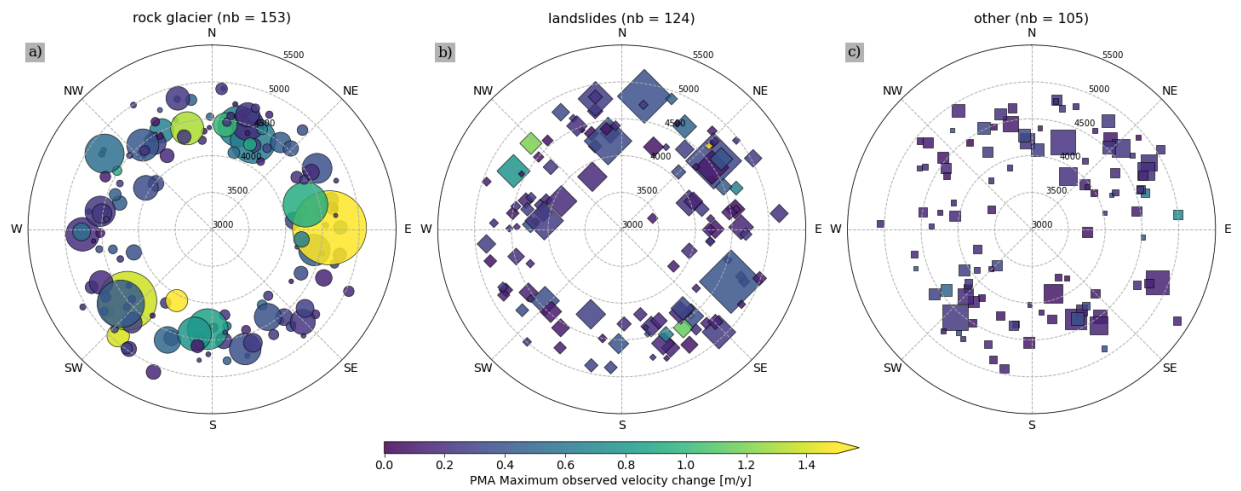


Figure S5. Distribution of PMA ranged by elevation and slope orientation: a) rock glaciers, b) landslides, c) others. Colorbar represents the Top 50% mean velocity for each PMA.

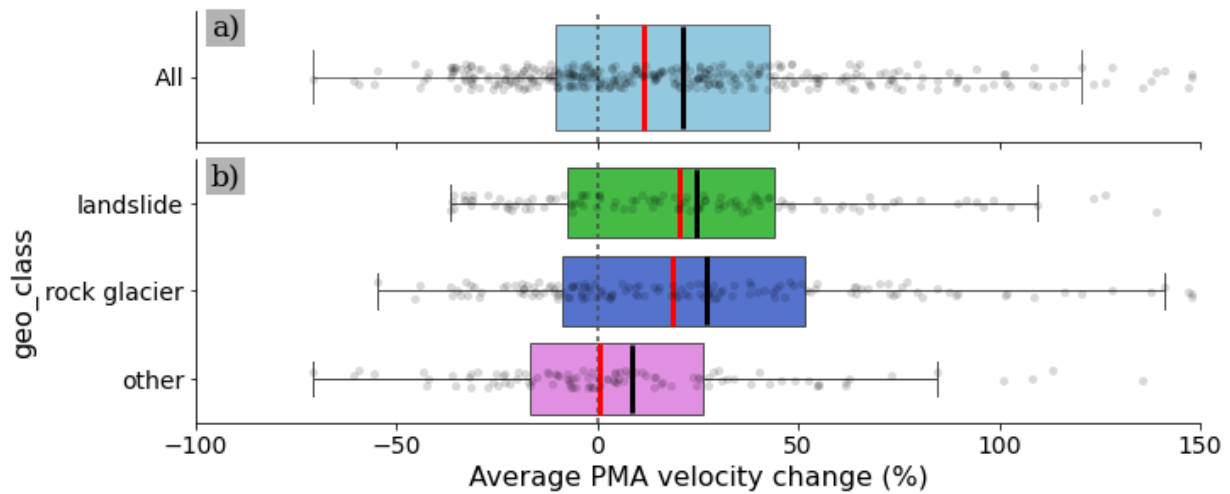


Figure S6. Boxplot showing average percentage of velocity change by PMA for the periods 2000-2014 and 2013-2024. Upper boxplot shows the distribution of the all PMA's. Lower boxplot show the distribution of PMA ordered by geomorphological classification. Red and black lines represent the median and average for each dataset, respectively.

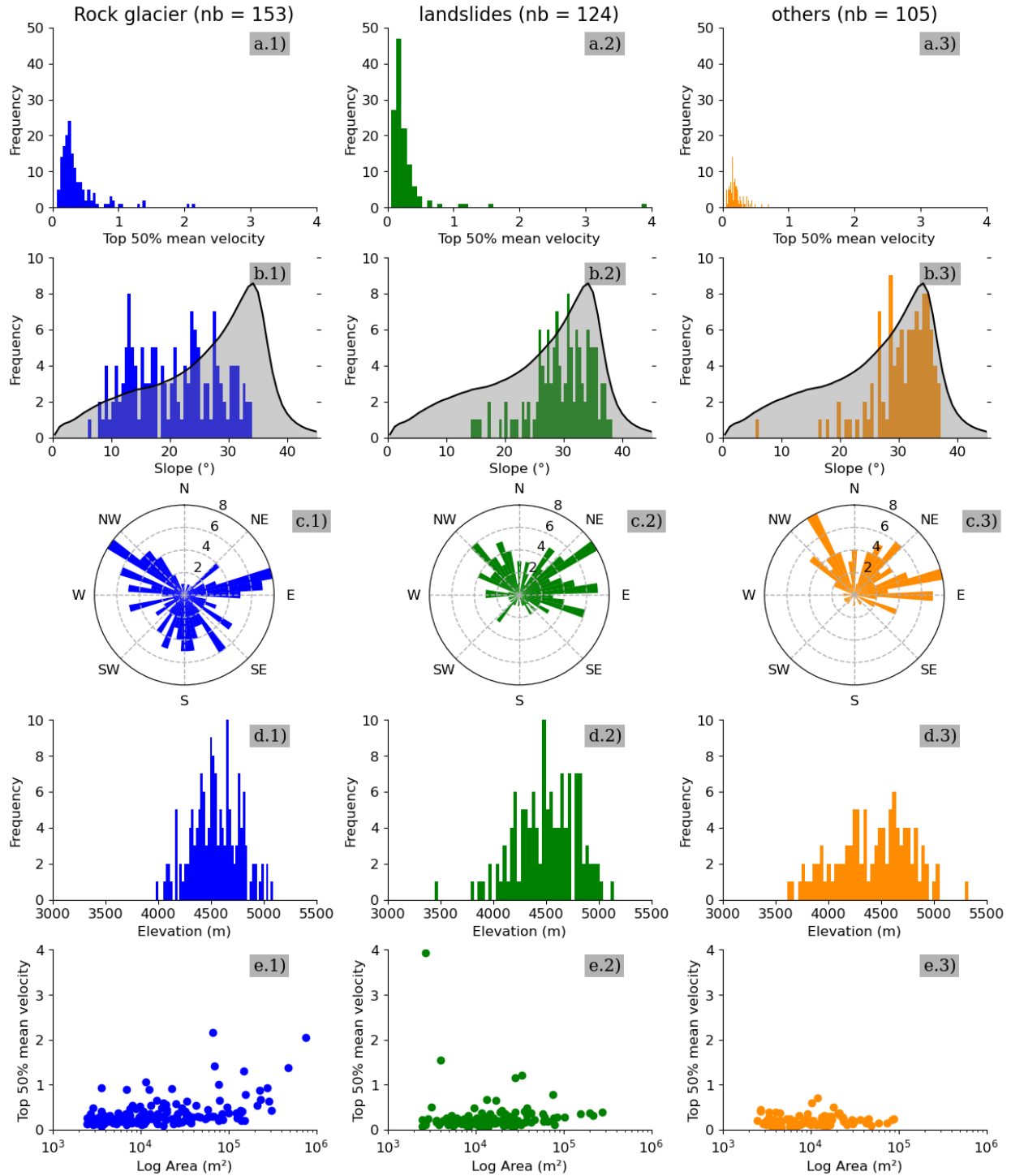


Figure S7. Comparison of the PMA distribution for rock glacier, landslides and other geomorphological class vs topographical context. a) Top 50% mean velocity; b) mean slope; c) slope orientation; d) elevation and e) distribution between Top 50% mean velocity PMA surface.

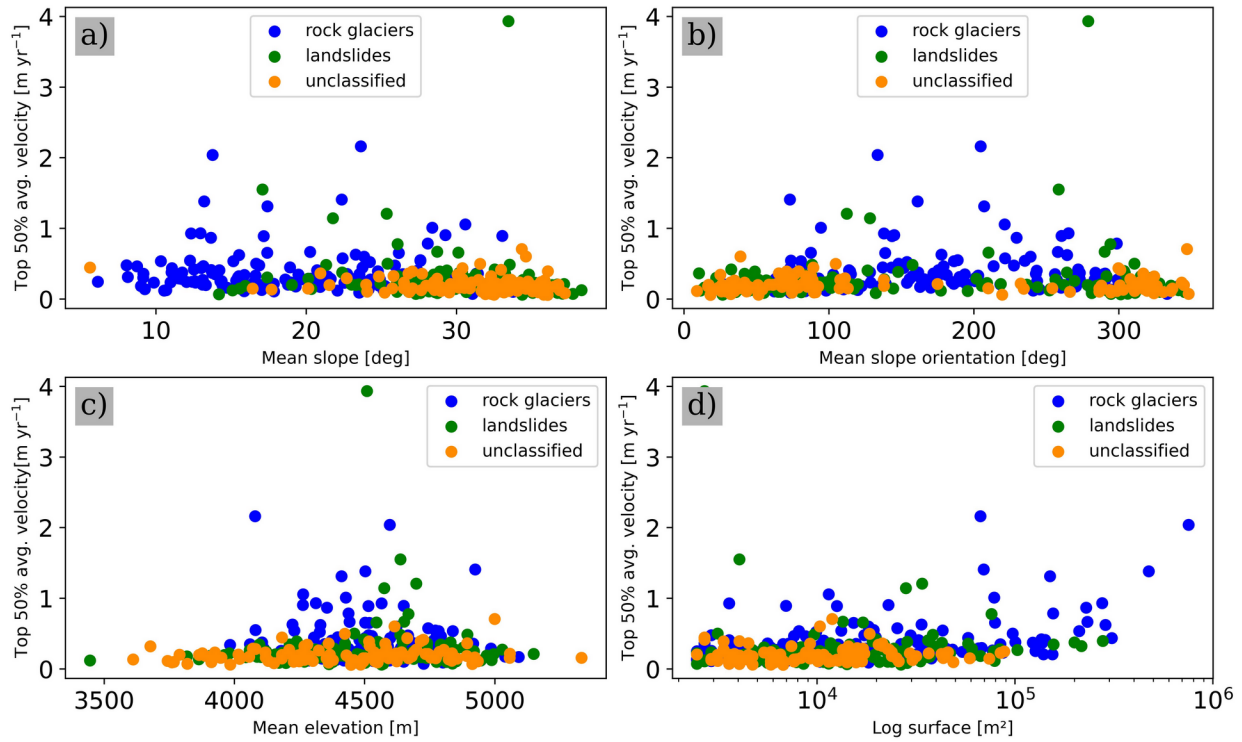


Figure S8. Comparison of the Top 50% mean velocity for each PMA for rock glacier, landslides and other geomorphological class vs topographical context. a) mean slope; b) slope orientation; c) elevation and d) PMA surface.

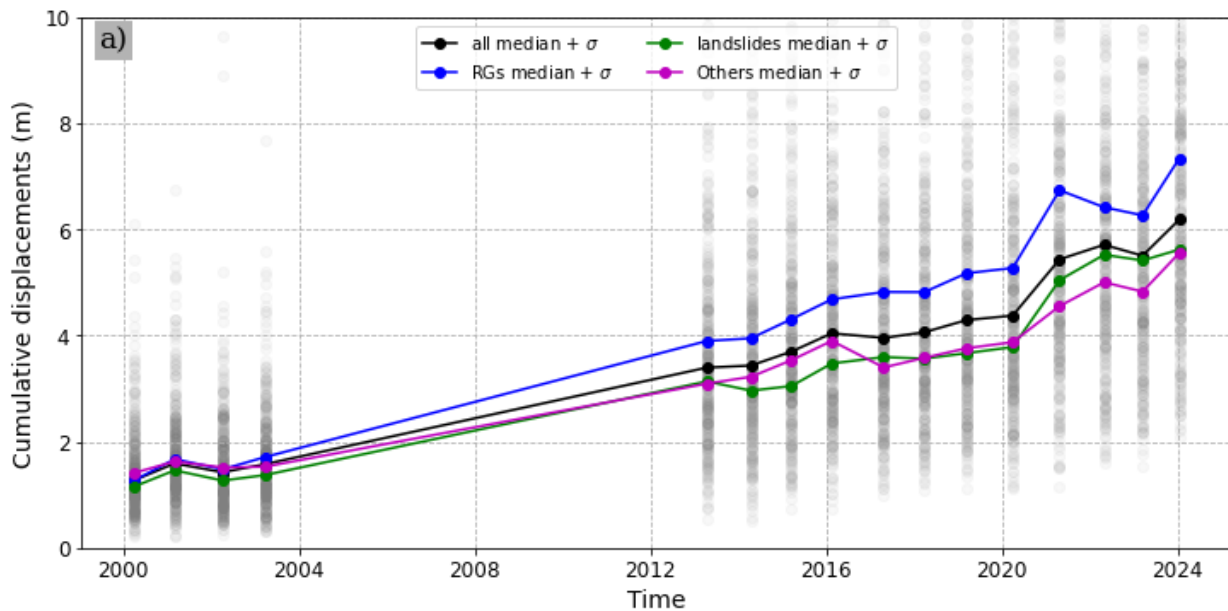


Figure S9. Time series of displacements for all filtered PMA. Grey dots shows the top 50% median surface velocity for each PMA. Blue, green, magenta and black dots and lines, shown the top 50% median surface velocity for each class (rock glaciers, landslide, others and all PMA dataset, respectively).

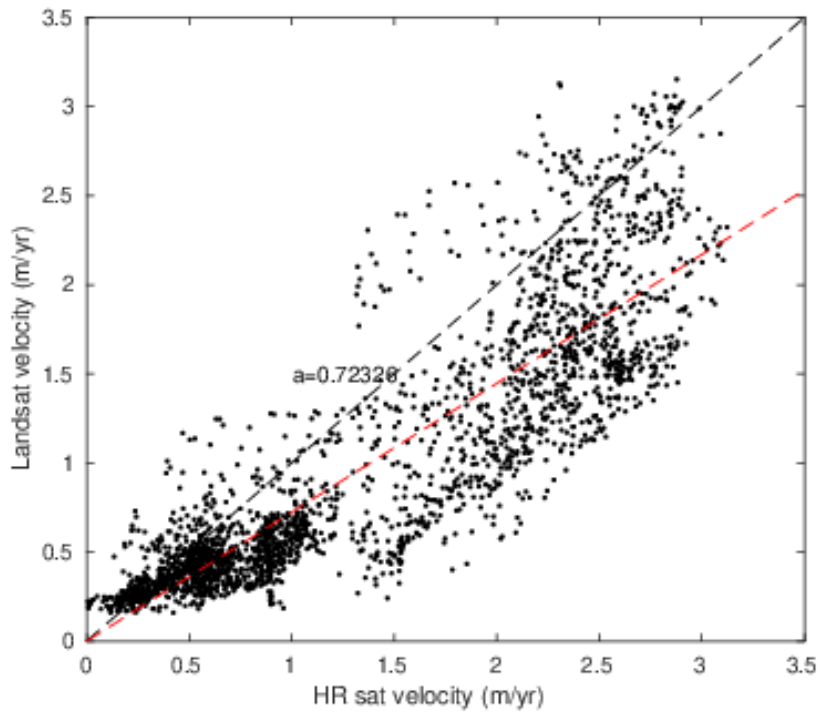


Figure S10. Pixel-to-pixel comparison of both HR dataset vs L7/8 dataset over Tapado complex area and largo rock glacier.

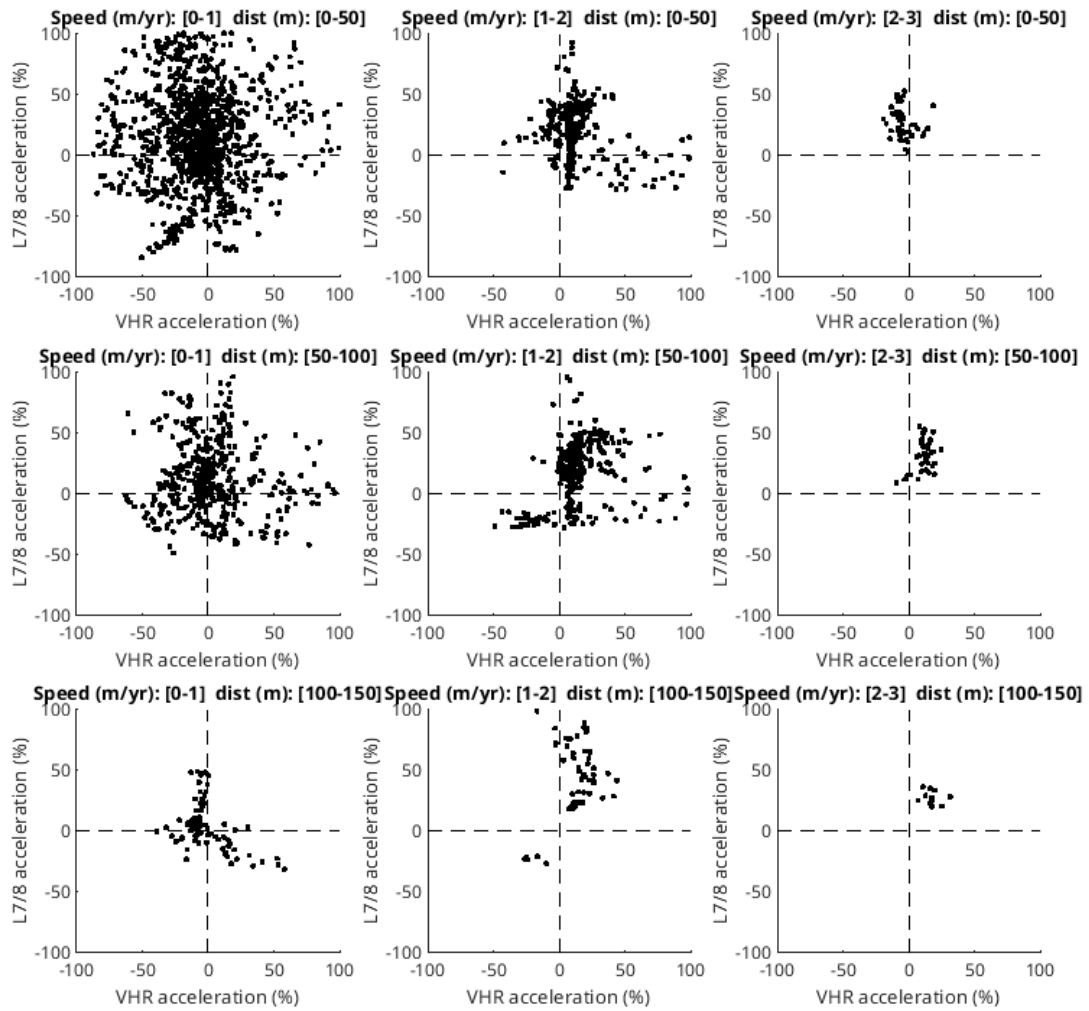


Figure S11. Pixel-by-pixel comparison of velocity changes between two time periods 2000 - 2013 & 2013 - 2020 for both L7/8 & VHR datasets on Tapado Complex and Largo Rock Glacier. Horizontally arranged subplots show common pixels classified by range of velocity (0-1, 1-2, 2-3 m a⁻¹) and vertically arranged velocity taken at a distance from the boundary (0-50, 50-100, 100-150 m) to avoid lateral effects.

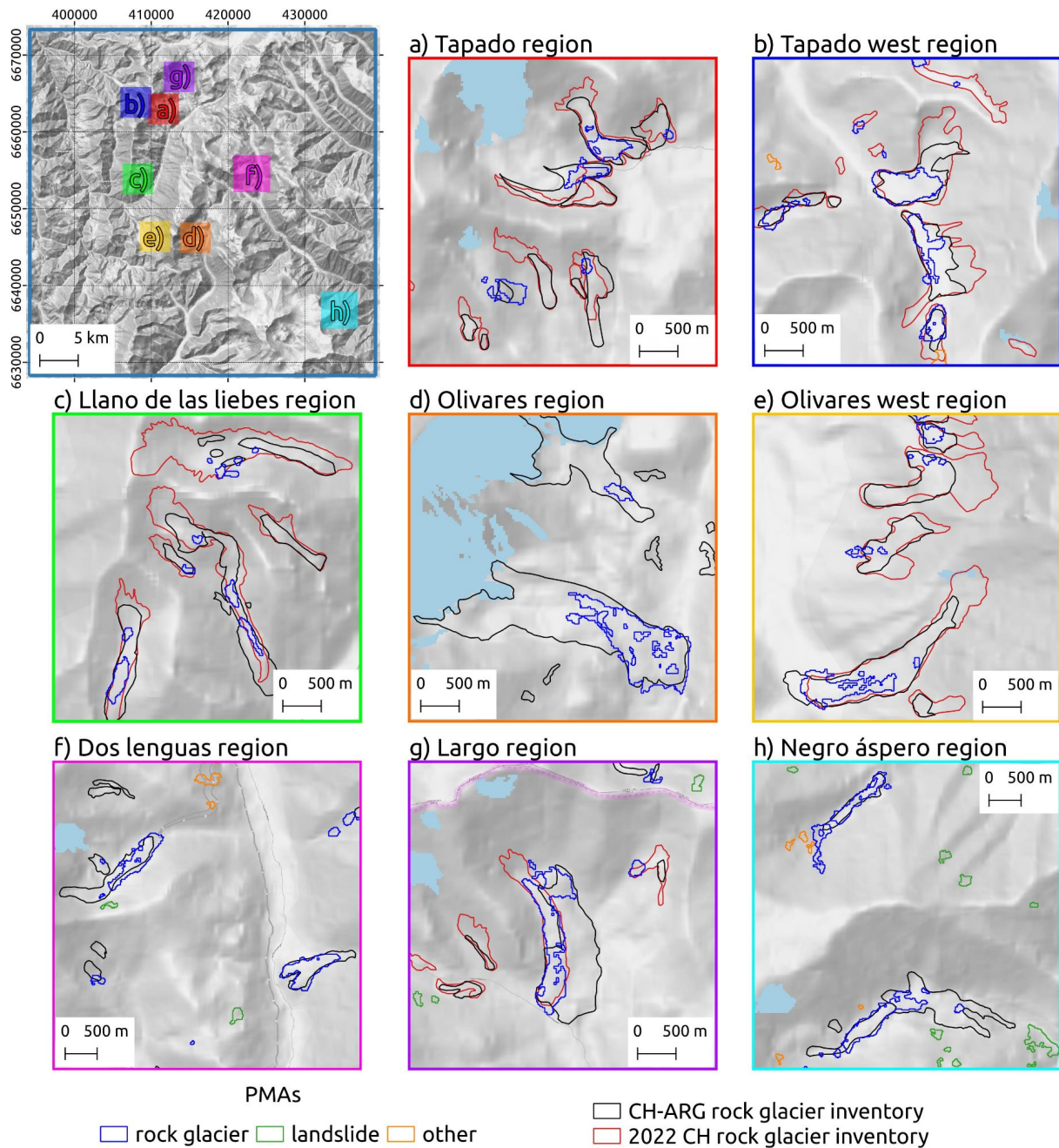


Figure S12. Comparison between existing rock glacier inventories and PMA detection. Black polygons represent Chile and Argentina 2013 (DGA, 2013) and 2018 (IANIGLA, 2018) rock glacier outlines. Red polygons shows the updated version of the rock glacier inventory for Chile (DGA, 2022).

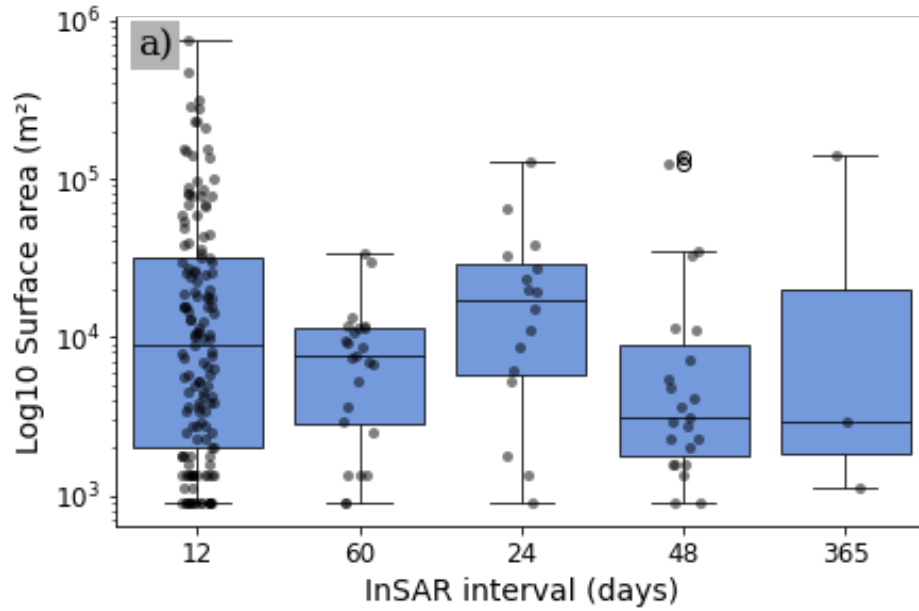


Figure S13. The box plot shows the surface distribution of PMAs ordered by the number of days of the interferograms on where the PMA is also detected.

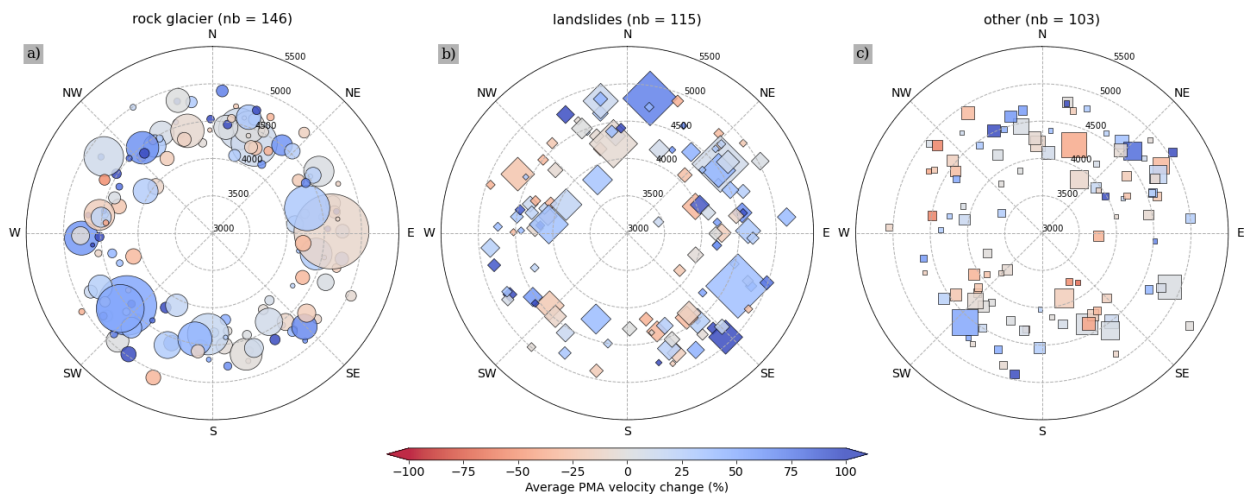


Figure S14. Polar plot showing the distribution of each PMA ordered by geomorphological class. Points are ordered by slope orientation and 500m altitudinal bins. Colorbar show the percentage of velocity change and size of symbol represents the PMA surface.

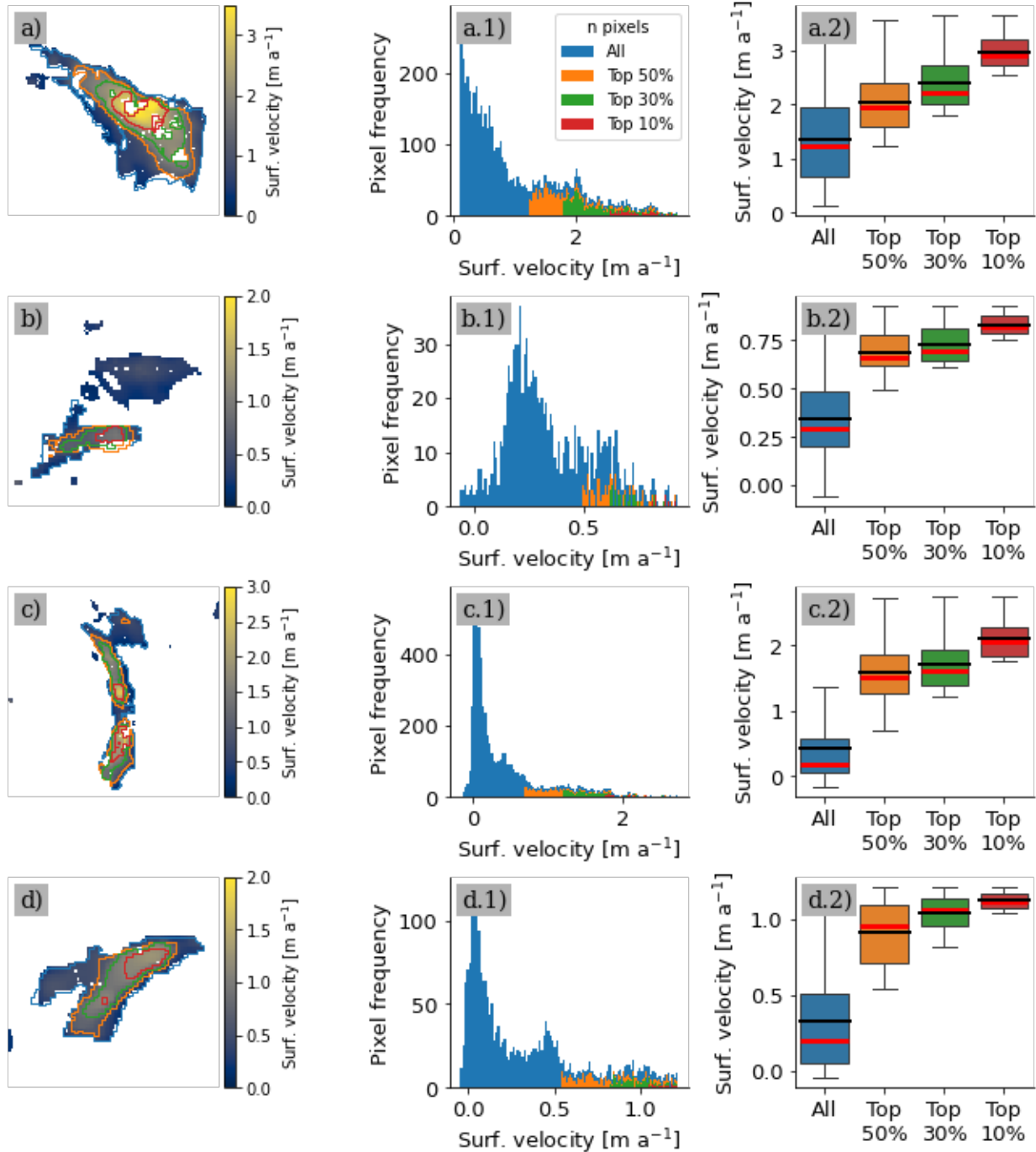


Figure S15. Representativity of spatial average statistics for four landforms: (a) Olivares debris ice complex, (b) Tapado complex, (c) Largo rock glacier, and (d) Dos Lenguas rock glacier. Subplots labeled with a suffix *.1 illustrate the pixel distribution for each metric used in this study: All (blue), Top 50% (orange), Top 30% (green), and Top 10% (red) average velocity. Subplots with a suffix *.2 display boxplots representing surface velocity for each landform, showing the variability and representativity of the computed metrics. Red and black lines in the boxplot represent the median and mean values respectively.

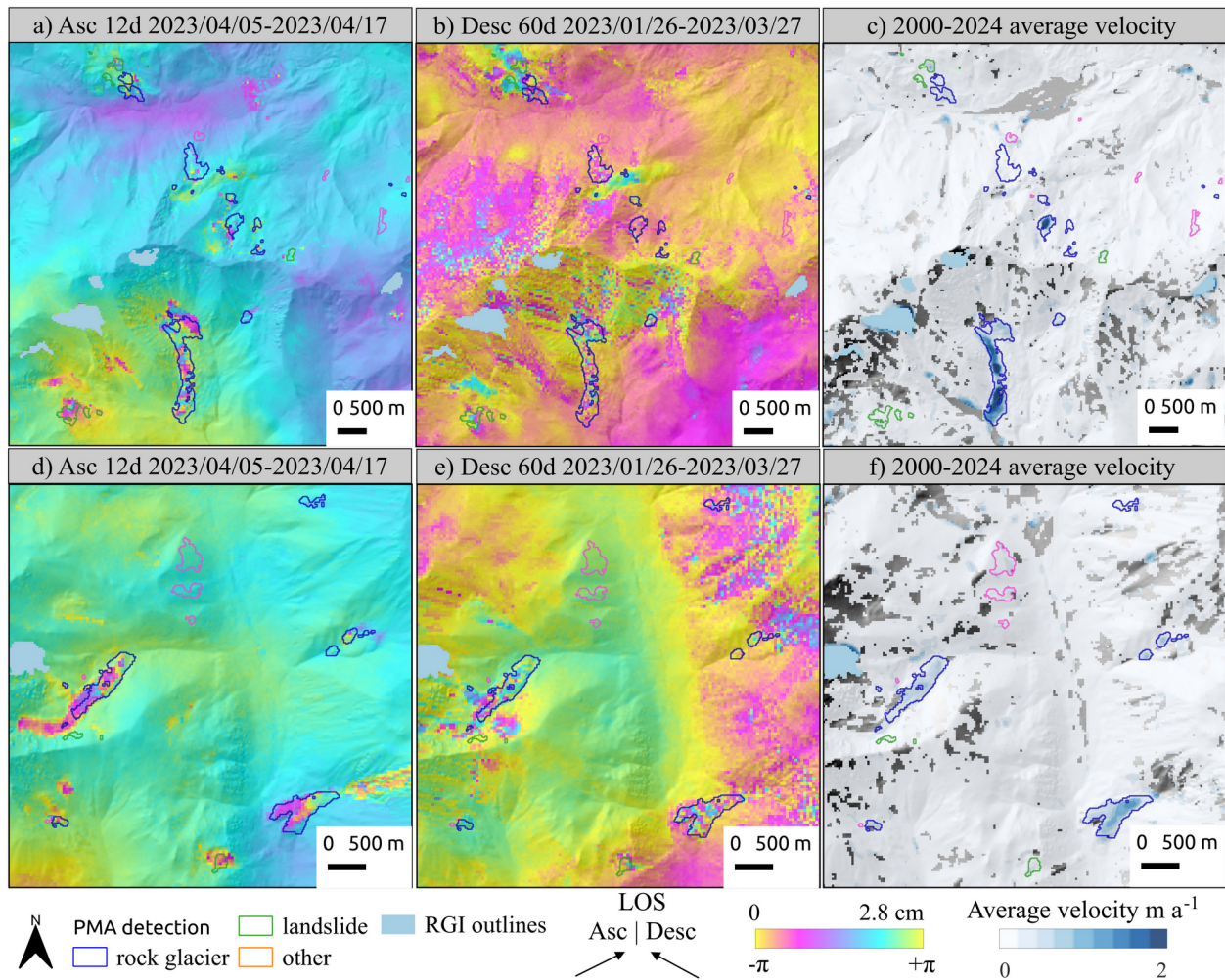


Figure S16. Comparison between Sentinel-1 wrapped interferograms at 12 and 60 days of interval and average surface velocity fields, in two small regions in the Central Andes.

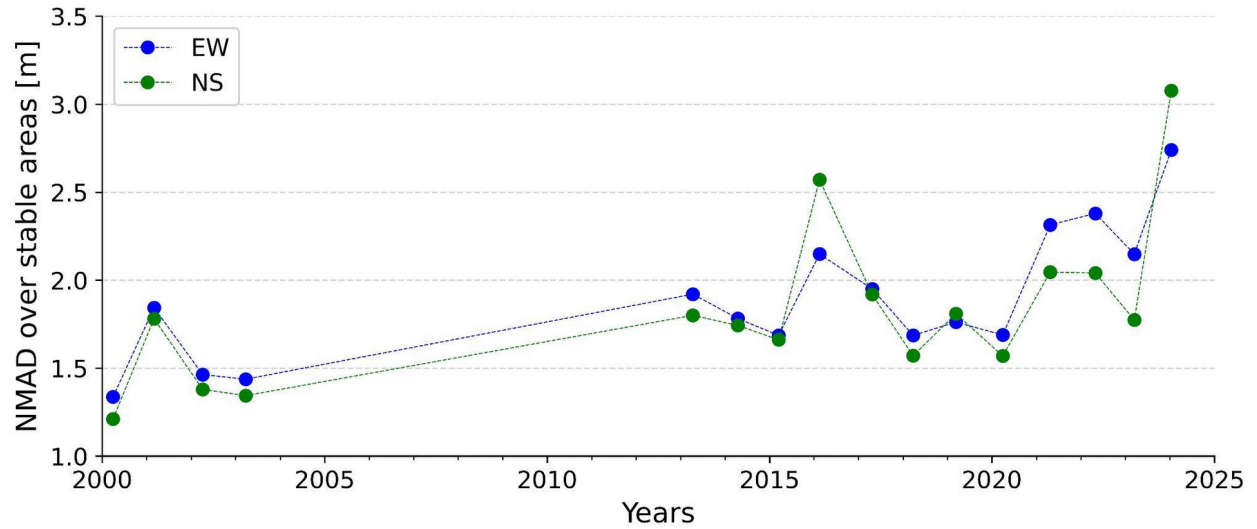


Figure S17. Annual NMAD values for the east-west (EW) and north-south (NS) components over stable areas for the L7/8 dataset. Figure S4 presents the stable area map of the study area used for NMAD computing.

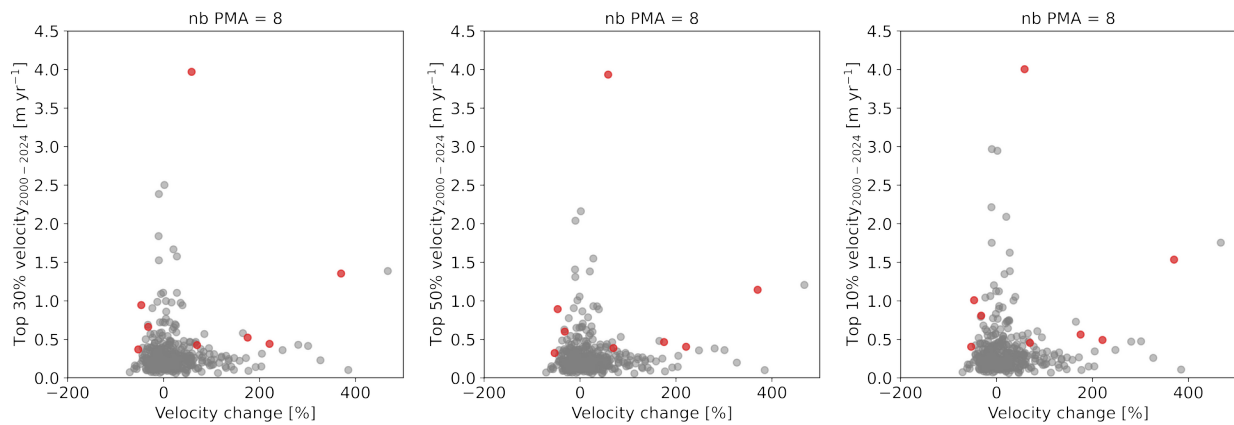


Figure S18. Comparison between velocity change (Eq. 1) and Top 50%, 30% and 10% average velocity over 24 years. Grey dots shows the entire PMA dataset ($n = 382$) and red dots shows PMAs when velocity change is greater than respective uncertainty (σV_{change} ; Eq. 2).

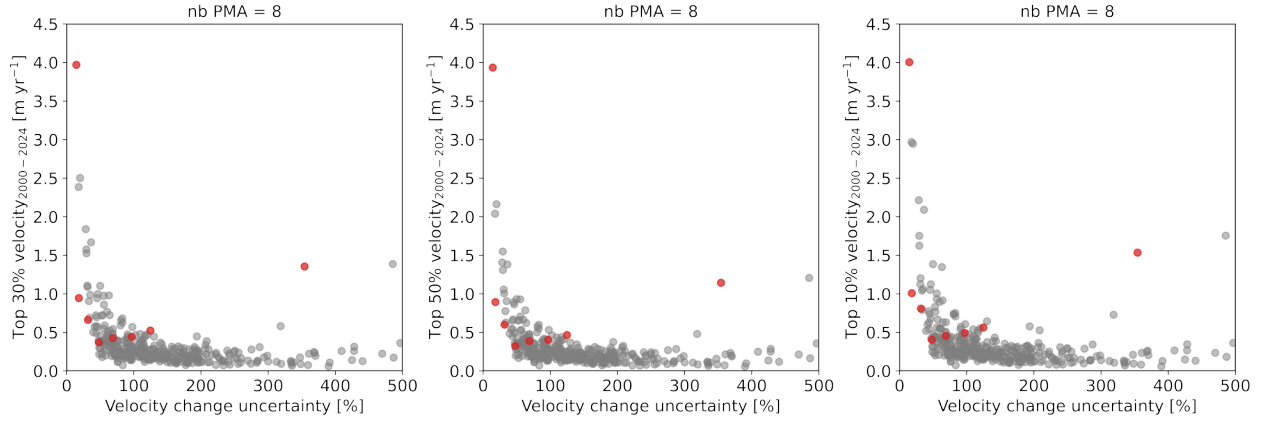


Figure S19. Comparison between velocity change uncertainty (Eq. 2) and Top 50%, 30% and 10% average velocity over 24 years. Grey dots shows the entire PMA dataset ($n = 382$) and red dots shows PMAs when velocity change is greater than respective uncertainty (σV_{change} ; Eq. 2).

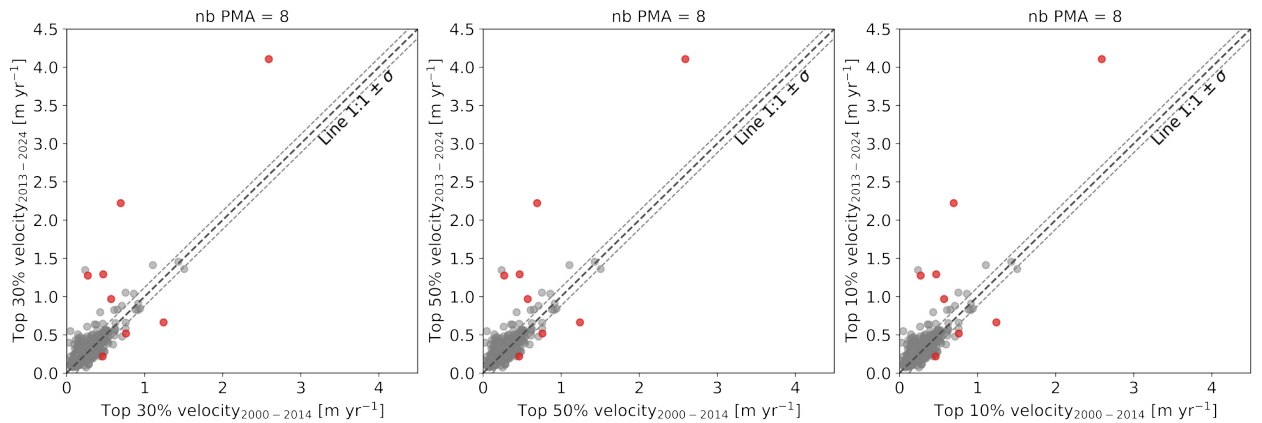


Figure S20. Comparison between average velocity for two periods $V_1 = 2000-2014$ and $V_2 = 2013-2024$. Grey dots shows the entire PMA dataset ($n = 382$) and red dots shows PMAs when velocity change is greater than respective uncertainty (σV_{change} ; Eq. 2).